atmosphere

MDPI

Article

Patterns and Controls of the Latent and Sensible Heat Fluxes in the Brazilian Pampa Biome

Gisele Cristina Dotto Rubert [1], Vanessa de Arruda Souza [1], Tamíres Zimmer [1], Gustavo Pujol Veeck [1], Alecsander Mergen [1], Tiago Bremm [1], Anderson Ruhoff [2], Luis Gustavo Gonçalves de Gonçalves [3] and Débora Regina Roberti [1,*]

[1] Departamento de Física, Universidade Federal de Santa Maria (UFSM), Santa Maria 97105-900, RS, Brazil; girubert@gmail.com (G.C.D.R.); v.arruda.s@gmail.com (V.d.A.S.); tamires.zimmer@ufsm.br (T.Z.); gustavo.veeck@acad.ufsm.br (G.P.V.); alecsander.mergen@acad.ufsm.br (A.M.); bremm.tiago@gmail.com (T.B.)

[2] Instituto de Pesquisas Hidráulicas, Universidade Federal do Rio Grande do Sul (UFRGS), Porto Alegre 91501-970, RS, Brazil; anderson.ruhoff@ufrgs.br

[3] Centro de Previsão de Tempo e Estudos Climáticos (CPTEC), Instituto Nacional de Pesquisas Espaciais (INPE), Cachoeira Paulista 12630-000, SP, Brazil; luis.goncalves@inpe.br

* Correspondence: debora@ufsm.br

Abstract: Energy and water exchange between the surface and the atmosphere are important drivers to Earth's climate from local to global scale. In this study, the energy dynamic and the biophysical mechanisms that control the energy partitioning over a natural grassland pasture over the Brazilian Pampa biome are investigated using two micrometeorological sites located 300 km apart, in Southern Brazil. The latent heat flux, *LE*, was the main component of the energy balance in both autumn-winter (AW) and spring-summer (SS) periods. Annually, approximately 60% of the available energy is used for evapotranspiration (*ET*). However, the Bowen ratio presents seasonal variability greater in AW than SS. Global radiation, *Rg*, is the atmospheric variable controlling *LE* and sensible heat flux, *H*. Hysteresis curves in the daily cycle were observed for *ET* and surface conductance, *Cs*, regarding the environmental variables, net radiation, vapor pressure deficit, and air temperature. Among the variables analyzed in the Pampa biome, surface conductance and evapotranspiration respond more strongly to the vapor pressure deficit. The hysteresis cycles formed by *ET* and conductance show a substantial biophysical control in the *ET* process. The results obtained here allowed a comprehension of the biophysical mechanisms involved in the energy partition process in natural grassland. Therefore, this study can be used as a base for research on land-use changes in this unique ecosystem of the Pampa biome.

Keywords: energy balance; evapotranspiration; surface conductance; aerodynamic conductance; grassland

Citation: Rubert, G.C.D.; de Arruda Souza, V.; Zimmer, T.; Veeck, G.P.; Mergen, A.; Bremm, T.; Ruhoff, A.; de Gonçalves, L.G.G.; Roberti, D.R. Patterns and Controls of the Latent and Sensible Heat Fluxes in the Brazilian Pampa Biome. *Atmosphere* **2022**, *13*, 23. https://doi.org/10.3390/atmos13010023

Academic Editor: Gianni Bellocchi

Received: 31 October 2021
Accepted: 21 December 2021
Published: 24 December 2021

1. Introduction

Understanding the main mechanisms responsible for the partitioning of net radiation (*Rn*) energy used to heat the atmosphere (sensitive heat flux, *H*), the subsoil (soil heat flux, *G*), and changing the water's physical state (latent heat flux, *LE*, or evapotranspiration, *ET*) is essential for climate studies and weather forecasts, as necessary on providing useful information to improve water resources management. For example, the *ET* process is linked directly to energy partitioning, stomatal conductance, carbon exchange, and water availability through the water-use efficiency by the plants acting as a key regulator of the ecosystems processes [1–3]. Grasslands are one of the most widespread vegetation types, accounting for approximately 32% of the planet's natural vegetation [4], making them important when studying the global vegetation dynamics and responses of ecosystem physiology to environmental change.

The Pampa biome, in southern Brazil, which is dominated by grasses, plays an essential role in livestock industry in the region [5,6] and is responsible for over 90% of the feeding

source for cattle and sheep herds [7]. The areas have been used inappropriately, through an excessive load of animals, which has caused environmental impacts due to vegetation cover loss, invasion of exotic species, and soil erosion [8,9]. Studies have shown that pasture ecosystem degradation not only alters its structure and ecosystem productivity but also affects surface–atmosphere interactions, changing heat and water transport [10–13].

Studies have shown that grasslands are more vulnerable than other ecosystems to warming climate changes [14,15]. Knapp e Smith [14] found that increases in primary productivity in wet years were much more pronounced than reductions in productivity during drought years in grassland continental ecosystems in the United States. Rajan et al. [16] showed that the variability of the energy balance partitioning is directly affected by water availability, finding that *LE* consumed most of the available energy. However, when the soil moisture remained low, *H* predominated the partition, which resulted in less plant growth. The vegetation and climatic characteristics are determining patterns for defining local seasonality and the partition of available energy in grassland ecosystems [14–17].

Changes in the surface energy partitioning directly impact the water budget through evapotranspiration [17–21]. The accuracy in estimating the energy balance component, mainly *LE*, depends on effective measurements of the conductance parameters. Surface (*Cs*) and aerodynamic (*Ca*) conductance represent a coupling factor between these processes, allowing a better understanding of the energy and mass exchanges between ecosystems and the atmosphere [22–28]. Some studies on vegetation conditions and environmental variables have been reported, showing the relationship between the conductance and meteorological variables [29–31] with different responses to changes in environmental factors during the processes of stomatal opening and closing [32–34]. The more realistic parameterizations of *Ca* and *Cs* have been highlighted from an observational and modeling point of view [35–37]. Thus, to understand the process of water transfer in an ecosystem, specific studies of *Cs* and *Ca* are necessary [38].

The Pampa biome is still not well characterized in terms of surface–atmosphere interaction [39]. Understanding the average and dynamic annual conditions across the biome is essential to improve our knowledge of changes in vegetation and primary productivity due to anthropogenic and/or climatic causes. Knowing the spatial and seasonal variation of biosphere–atmosphere interactions, such as energy and water exchanges, becomes of great importance. This study aims to advance in the understanding of the annual and seasonal variability and the biophysical mechanisms that control the energy balance components in natural pasture areas over the Pampa biome in southern Brazil. Thus, the scientific questions addressed in this work regarding the native field of the Pampa biome are: (*i*) what is the energy partition in the ecosystem exchange processes? (*ii*) what are the meteorological variables that control sensible and latent heat fluxes? (*iii*) what are the seasonal and annual behavior of the surface and aerodynamic conductance? (*iv*) what are the most relevant meteorological variables for the representation of aerodynamic and surface conductances? To answer these questions, we used two years of data from two eddy covariance measuring sites, both located in the Pampa biome, Santa Maria and Pedras Altas, approximately 300 km apart.

2. Materials and Methods

2.1. Site Description

In this study, we analyzed energy surface fluxes and environmental data obtained from two experimental sites, Santa Maria and Pedras Altas, both in the Pampa biome, located in the Rio Grande do Sul state, Brazil (Figure 1). The climate is classified as Cfa, temperate, with hot summer and no dry season, according to the Köppen classification [40]. The vegetation in the Pampa biome is dominated by photosynthetic metabolism C3, but co-exist with C4 species, being one of the distinct characteristics of the South Brazilian grasslands. Both sites are within similar vegetation physiognomies in the Pampa, with a high diversity of grass species used as pasture for cattle.

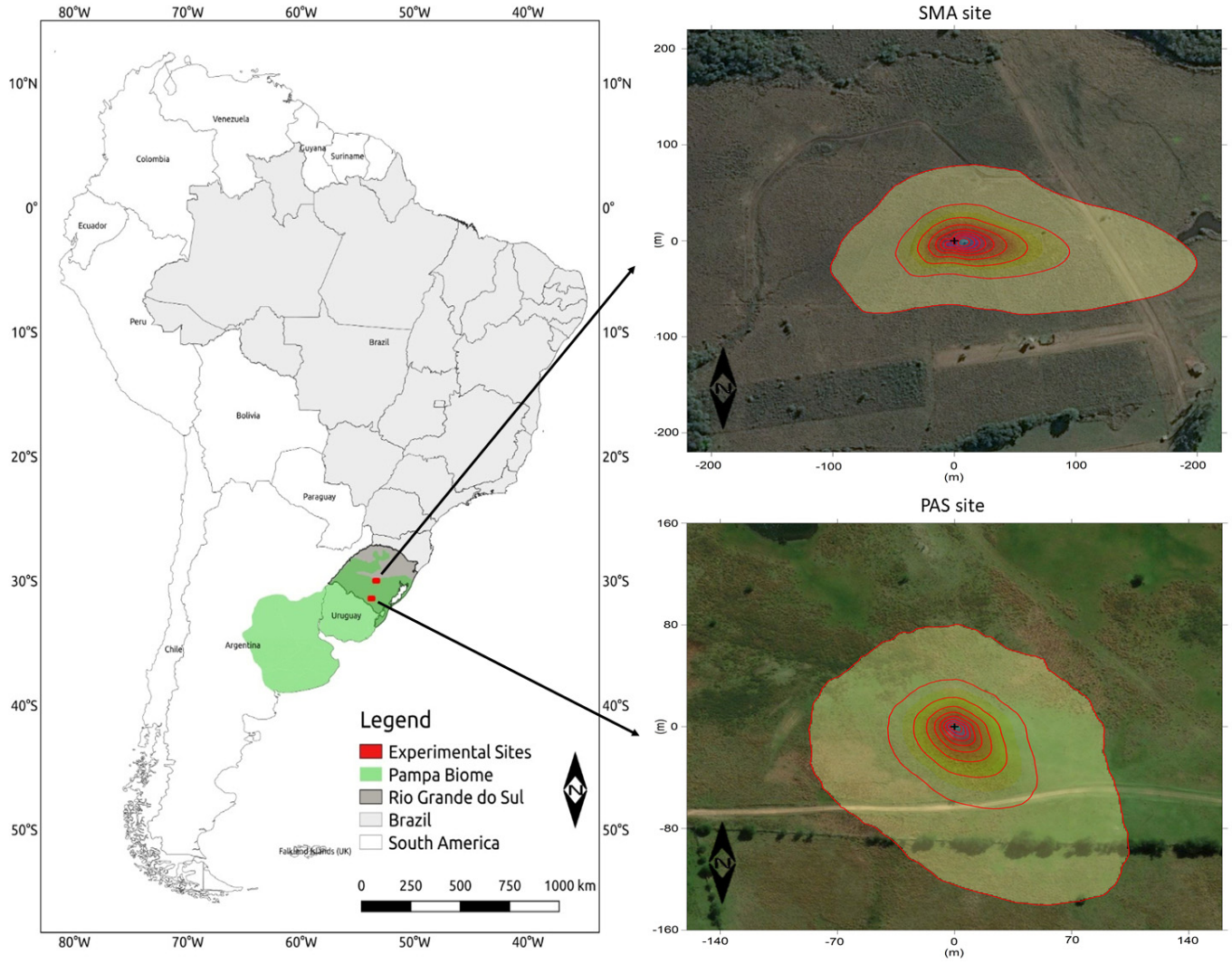

Figure 1. Location of the study areas in the Pampa biome—Santa Maria (SMA) and Pedras Altas (PAS). The footprint climatology (until 90%) of the flux measurements for both sites is presented in the right panel. The image of the area was not obtained in the period of the experiments analyzed in this study.

The Santa Maria site, SMA, (lat 29°43′27.502″ S; lon 53°45′36.097″ W, alt 88 m) is located in the municipality of Santa Maria, in an area of 24 ha of natural vegetation. The soil is classified as Eutrophic Haplossol, according to the exploratory soil map of the state of Rio Grande do Sul [41]. The textural class of soil is clay loam (47.12% sand; 16.90% clay; 35.97% silt), with field capacity, θ_{FC} = 0.34 m^3 m^{-3}; permanent wilting point θ_{WP} = 0.12 m^3 m^{-3}; soil porosity, θ_s = 0.46 m^3 m^{-3}; and soil bulk density, ρs = 1397 kg m^{-3}, measured at 0.5 m depth. The vegetation found in the study area is natural pasture with a predominance of *Andropogon lateralis*, *Axonopus affinis*, *Paspalum notatum*, and *Aristida laevis* [42], uniformly distributed in the study area [43].

The Pedras Altas site, PAS, (lat 31°43.556′ S; lon 53°32.036′ W, alt 395 m) is located in a private property in the municipality of Pedras Altas-RS. The soil is classified as Neosol and Cambisol [41], with rocky outcrops, and a sandy loam structural classification (59.30% sand; 0.81% clay; 39.89% silt). The soil properties measured at 0.5 m depth are θ_{FC} = 0.31 m^3 m^{-3}; θ_{WP} = 0.03 m^3 m^{-3}; soil porosity, θ_s = 0.44 m^3 m^{-3}; and soil bulk density, ρs = 1405 kg m^{-3}. The phytophysiognomy of the site has a predominance of grassland, mainly stoloniferous and rhizomatous species, such as *Axonopus affinis*, *Paspalum notatun*, *Aeristida laevis*, and

Iriantus angustifolium. More information regarding the soil type and vegetation for both sites can be found in Rubert et al. [39].

The phenology of vegetation at both sites was estimated using the EVI (Enhanced Vegetation Index) data time series with a spatial resolution of 250 m obtained from the MODIS sensor (Moderate Resolution Imaging Spectroradiometer, is the instrument aboard the NASA's *Terra satellite*) through the product MOD13Q1. The surface albedo was obtained from the MODIS sensor through the product BRDF/MCD43A (MODIS/Terra + Aqua BRDF and calculated albedo ("shortwave actual"), with spatial resolution of 500 m. The selected period was from 29 August 2014 to 15 October 2016, (every 16 days) for EVI and from 29 August 2014 to 7 October 2016, to surface albedo (every 8 days). These data comprise the same period of energy fluxes analyzed in this work.

2.2. Energy Fluxes and Meteorological Measurements

PAS and SMA experimental sites were equipped with flux towers measuring atmospheric variables and surface fluxes. The flux towers were equipped with the sensors described in Table 1. The eddy covariance method (EC) was used to estimate *LE* and *H* from 1 September 2014 to 1 September 2016, in both sites. Further details are described in [44–46].

Table 1. Sensors installed at the flux towers used in this study.

Variable	Sensor Model and Manufacturer/Sensor Type	Position (m)-Sites	Frequency
Wind speed components and air temperature	CSAT3, Campbell Scientifific Inc., Logan, UT, USA/3D sonic anemometer	2.5-PAS	10 Hz
	Wind Master Pro; Gill Instruments, Hampshire, UK/3D sonic anemometer	3.0-SMA (until 25 June 2016)	10 Hz
	IRGASON, Campbell Scientific Inc., Logan, UT, USA/Integrate 3D sonic anemometer and open path gas analyzer	3.0-SMA (after 25 June 2016)	10 Hz
H_2O concentration	LI7500, LI-COR Inc., Lincoln, NE, USA/Open path gas analyzer	2.5-PAS 3.0-SMA (until 25 June 2016)	10 Hz
	IRGASON, Campbell Scientific Inc., Logan, UT, USA/Integrate 3D sonic anemometer and open path gas analyzer	3.0-SMA (after 25 June 2016)	10 Hz
Air temperature (*Temp*) and relative humidity (*RH*)	HMP155, Vaisala, Finland/Thermohygrometer	2.5-PAS 3.0-SMA	1 min
Precipitation	TR525USW, Texas Electronics, Dallas, TX, USA/Pluviometer	2.5-SMA 2.0-SMA	1 min
Net radiation (*Rn*)	CNR4, Kipp & Zonen, Delft, The Netherlands/ Net Radiometer	3.0-SMA	1 min
	CNR2, Campbell Scientific Inc., Logan, UT, USA/ Net Radiometer	2.5-PAS	1 min
Global Radiation (*Rg*)	CNR4, Kipp & Zonen, Delft, The Netherlands/ Net Radiometer	3-SMA	1 min
	Li 200S Pyranometer—LI-COR, Lincoln, NE, USA/Pyranometer	2.5-PAS	1 min
Ground heat flux (*G*)	HFP01, Hukseflux Thermal Sensors B.V., Delft, The Netherlands/Thermopile	−0.10-PAS −0.10-SMA	5 min
Soil moisture (θ)	CS616, Campbell Scientific Inc., Logan, UT, USA/Water Content Reflectometer	−0.10-PAS −0.10-SMA	1 min
Soil Temperature (*Tsoil*)	T108, Campbell Scientific Inc., Logan, UT, USA/Thermometer	−0.05-PAS −0.05-SMA	1 min

The *LE* and *H* fluxes were estimated on a half-hour timescale using the EddyPro™ software, version 6.1, Li-Cor (Lincoln, Nebraska, EUA). Turbulent fluctuations were obtained in average per block and double rotation and correction for the effects of density [47]. The high-frequency spectral correction was based on mathematical formulations to model the flux and spectral properties that describe flux attenuations due to the instrumental configuration [48]. High and low pass filter corrections followed the methodology described by Moncrieff et al. [49] and Moncrieff et al. [50], respectively. Quality tests on fluxes followed the methodology described by Mauder and Foken [51]. The angle of attack correction for wind components was determined according to Nakai and Shimoyama [52]. For statistical analysis, the removal of spikes followed the method described by Vickers and Mahrt [53].

Physically inconsistent data were filtered in post-processing. Gaps in the time series of energy fluxes generated by the post-processing step or sensor malfunctions were filled using the method proposed by Reichstein et al. [54] with the REddyProc package. More details regarding the sensors, footprint measurement, surface flux processing, and gap-filling are described in Rubert et al. [39].

2.3. Components of the Energy Balance

The relationship between available energy $(Rn - G)$ and the turbulent fluxes $(H + LE)$ is often used as an indicator of the *H* and *LE* accuracy estimated by the eddy covariance method [55–57]. The slope of the linear regression between $(Rn - G)$ and $(H + LE)$ for the period evaluated was 0.75 for SMA and 0.72 for PAS, as analyzed and discussed by Rubert et al. [39]. In this work, the energy balance closure followed the methodology described by Foken et al. [57], in which the experimental Bowen ratio ($\beta = H/LE$) for each site was used to distribute the residual energy, *RES*, ($RES = Rn - G - H - LE$) between *LE* and *H*.

The evapotranspiration process is influenced mainly by the energy available on the surface, atmospheric demand for water vapor, vegetation physiological factors, and resistances imposed on the transfer of water vapor between the vegetation and the atmosphere. The Food and Agriculture Organization (FAO) recommends using the Penman–Monteith method to estimate evapotranspiration, according to the FAO Bulletin 56 [58]. The Penman–Monteith equation combines aerodynamic and thermodynamic aspects to describe water vapor transfer between the surface and the atmosphere. The latent heat flux using the Penman–Monteith equation (LE_{PM}) is defined by:

$$LE_{PM} = \left(\frac{\Delta(Rn - G) + \rho_a c_p \frac{(e_s - e_a)}{r_a}}{\left(\Delta + \gamma\left(1 + \frac{r_s}{r_a}\right)\right)} \right) \quad (1)$$

where Rn (W m^{-2}) is the net radiation, G (W m^{-2}) is the soil heat flux, ρ_a (kg m^{-3}) is the mean air density at constant pressure, c_p (J kg^{-1}K^{-1}) is the specific heat of air at constant pressure, e_s (kPa) is the saturated water vapor pressure, e_a (kPa) is the water vapor pressure of the air, $(e_s - e_a)$ (kPa) is the air vapor pressure deficit (VPD), Δ (kPa °C^{-1}) is the slop of the saturation vapor pressure temperature relationship, γ (kPa) is the psychometric constant; r_s (s m^{-1}) is the surface resistance, r_a (s m^{-1}) is the aerodynamic resistance. Equation (1) results in hourly average values of LE_{PM} (W m^{-2}). The conversion to daily evapotranspiration (mm d^{-1}) (or hourly (mm h^{-1})) is done using the daily average (hourly) of LE_{PM} multiplied by the conversion factor of 0.0353 (0.0014). The same procedure is performed with the experimental *LE* after the energy balance closure to estimate the actual *ET*. In this work, the surface conductance was indirectly estimated by inverting the Penman-Monteith model (Eq. 1) using LE obtained by EC method:

$$\frac{1}{C_s} = r_s = \frac{r_a}{\gamma}\left[\frac{\Delta(R_n - G) + \rho_a c_p C_a (VPD)}{LE} - (\Delta + \gamma)\right] \quad (2)$$

Ca, which represents the intensity of vertical turbulence, close to the surface that carries heat and water vapor between the soil surface and the overlying atmosphere, was estimated according to Campbell and Norman [59], correcting the atmospheric stability.

$$\frac{1}{C_a} = r_a = \frac{1}{u_* \rho_a k \left[ln\left(\frac{z-d}{z_{om}}\right) + \Psi_m \right]} \left[ln\left(\frac{z-d}{z_{om}}\right) + \Psi_m \right] \left[ln\left(\frac{z-d}{z_{ov}}\right) + \Psi_v \right] \quad (3)$$

where u_* is the friction velocity, k is the Von Kármán constant (0.41), z is the height where the wind speed was measured, d is the zero-plane displacement, z_{om} (m) is the roughness length governing momentum transfer, calculated as 0.1 of the grass height, z_{ov} (m) is the roughness length governing the transfer of heat and vapor, calculated as 0.1 of z_{om}. Functions Ψ_m and Ψ_v correspond to the stability correction factors for the momentum and sensible heat, respectively.

The most used method to study atmospheric stability conditions is the stability parameter ζ, as described by Campbell and Norman [59], estimated from the convection rate that produces mechanic turbulence in the air.

$$\zeta = -\frac{kgzH}{\rho_a c_p T_{emp} (u_*)^3} \quad (4)$$

where g (m s^{-2}) is the gravity acceleration, $Temp$ (°C) is the air temperature, and others as described above. Stable atmosphere corresponds to positive values of ζ, unstable to negative values of ζ, and atmospheric neutrality to values within the interval $0 < \zeta < |0.0325|$ [60].

The equations for functions Ψ_m and Ψ_v to correct the atmospheric stability proposed by Campbell and Norman [59] are:

- For atmospheric instability:

$$\Psi_v = -2\, ln\left[\frac{1 + (1 - 16\zeta)^{\frac{1}{2}}}{2}\right] \quad (5a)$$

$$\Psi_m = 0.6\, \Psi_v \quad (5b)$$

- For atmospheric stability:

$$\Psi_m = \Psi_v = 6\, ln(1 + \zeta) \quad (5c)$$

3. Results and Discussion

The analysis of the results was separated into two parts: one based on the entire period of data available and the second on two sub-periods, autumn-winter (AW), from April to September, and spring-summer (SS), from October to March.

3.1. Meteorological and Surface Conditions

Daily cycle of *Rg*, *Temp*, *VPD*, and wind velocity (*u*) for SMA and PAS sites are shown in Figure 2. The entire period (two years of data) for *Rg* is very similar for both sites, with a slight difference in AW and SS, being the values greater in SMA in AW and smaller in SS than PAS values (Table 2). SMA presents higher *Temp* and *VPD* throughout the daily cycle than PAS (the same is seen in Table 2 for *Temp*). *u* is always stronger in PAS, mainly in night periods; however, the wind speed presents the same pattern in AW and SS for each site. During SS the values of *Prec* were greater in both sites. In the period 2015/2016 PAS had the lowest accumulated annual precipitation. Despite an accumulated difference in rainfall during some periods, *Prec* was well distributed throughout the year without water deficit. The soil moisture measurements in SMA showed higher values than in PAS, except for the SS period. As expected, *Tsoil* was greater in SS. When *Tsoil* was analyzed for the entire period it presented the same value of 19.3 °C in both sites (Table 2).

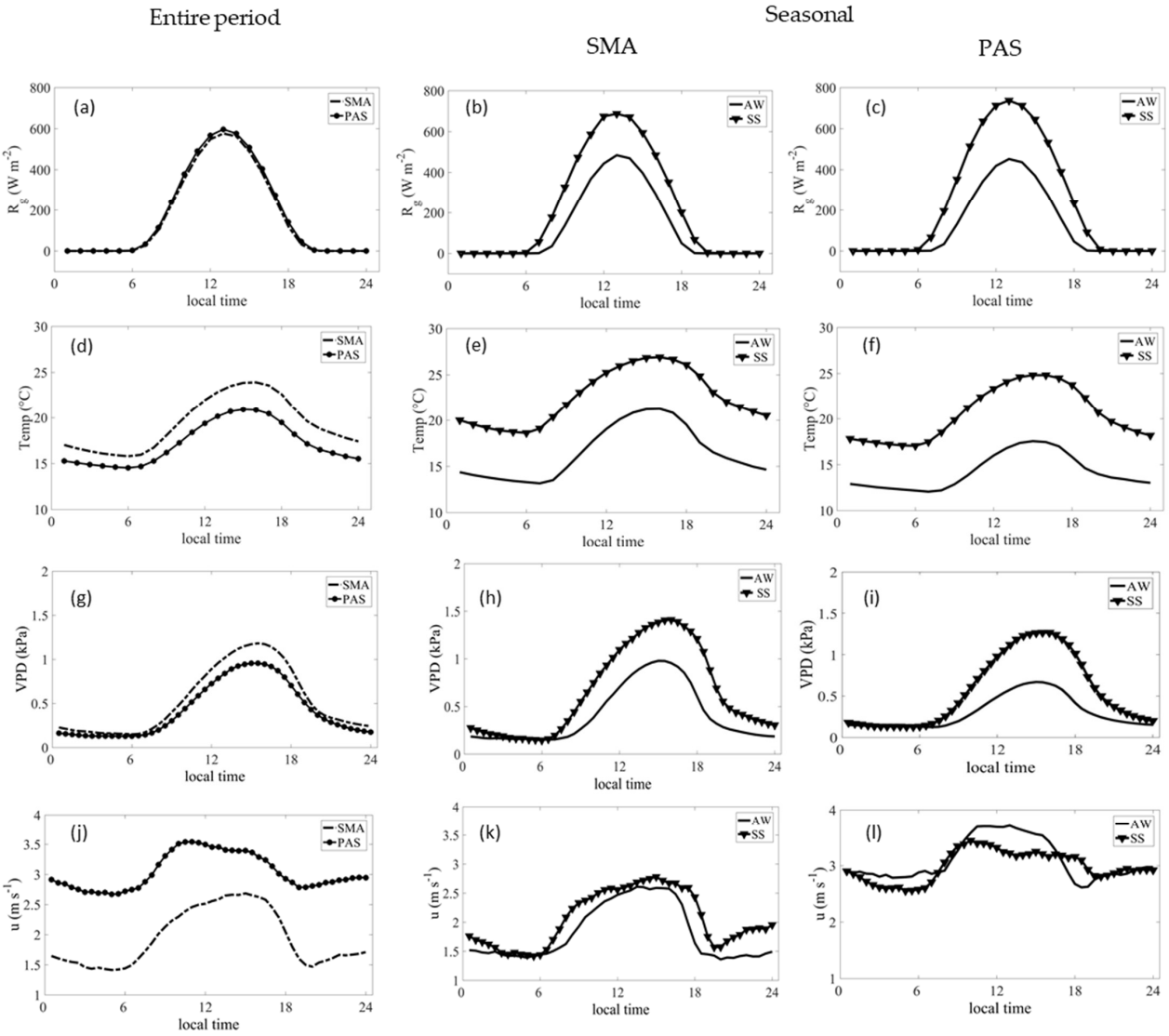

Figure 2. Daily cycles of meteorological variables: solar radiation (*Rg*, W m^{-2}) (**a**–**c**); air temperature (*Temp*, °C) (**d**–**f**); vapor pressure deficit (*VPD*, kPa) (**g**–**i**); wind velocity (*u*, m s^{-1}) (**j**–**l**); on the left column for the entire study period, on central for SMA in the AW and SS periods, and the right for PAS in AW and SS periods.

Figure 3 shows the surface albedo and the EVI. The mean albedo value was 0.15 for both sites during the analyzed period, with lower values in AW. Maximum values occurred in January, February, and March 2016 (in SS), reaching 0.18 for the SMA site. The average EVI values for this period are very similar between both sites, with 0.39 for SMA and 0.38 for PAS. Seasonality for EVI was more pronounced, showing the influences of the canopy and atmosphere, with minimum values observed in the AW, suggesting a slightly lower photosynthetic activity.

Table 2. Average of air temperature (*Temp*), solar radiation (*Rg*), accumulated precipitation *(Prec*), soil humidity (θ), soil temperature (*Tsoil*), energy balance components (*Rn*, *LE*, *H*, *G*), and Bowen ratio (β) for the Pampa biome, at the SMA and PAS sites.

		Site	*Temp* (°C)	*Rg* (W m^{-2})	*Prec* *(mm)*	θ (m^3 m^{-3})	*Tsoil* (°C)	R_n (W m^{-2})	*LE* (W m^{-2})	*H* (W m^{-2})	*G* (W m^{-2})	β
AW		SMA	16.2	127.2	1813	0.24	16.6	69.7	48.4	26.1	−4.5	0.54
		PAS	13.9	123.9	1359	0.20	15.7	57.2	44.1	19.0	−4.6	0.43
SS		SMA	22.6	226.3	2036	0.17	22.1	148.4	105.5	42.1	0.6	0.40
		PAS	19.9	243.4	1919	0.20	23.2	145.1	108.8	35.2	2.2	0.33
Annual	2014/2015	SMA	19.8	183.1	1824	0.23	19.8	114.1	80.8	34.9	−1.6	0.43
		PAS	17.6	192.4	1723	0.17.	19.8	105.9	78.4	28.9	−0.2	0.37
	2015/2016	SMA	18.7	171.0	2025	0.21	18.2	104.4	73.2	33.2	−2.1	0.45
		PAS	16.2	176.7	1555	0.19	18.7	97.2	75.6	25.3	−2.1	0.33
Entire period		SMA	19.4	177.1	3849	0.22	19.3	109.4	77.1	34.1	−1.8	0.44
		PAS	16.9	184.5	3278	0.18	19.3	101.6	77.1	27.0	−1.1	0.35

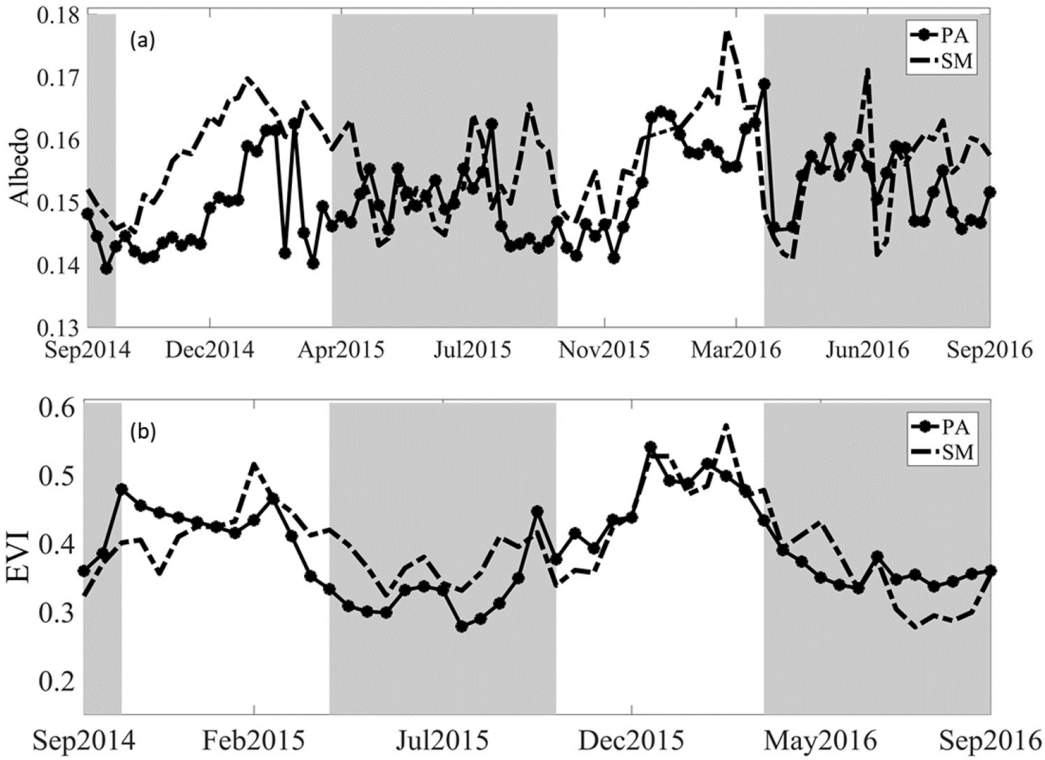

Figure 3. (**a**) Surface albedo and (**b**) EVI index for the SMA and PAS sites. The hatched areas represent the autumn-winter (AW) period.

3.2. Energy Balance Components

The seasonal and interannual variability of the energy balance components is presented in Figure 4 and Table 2. A well-characterized seasonal pattern is present in *Rn*, *H*, and *LE* for both sites. Daily variability of *Rn*, *LE*, and *H* was lower in AW and higher in SS. *H* presented a low amplitude of seasonal variation, while *LE* presented strong seasonality, similar to *Rn*.

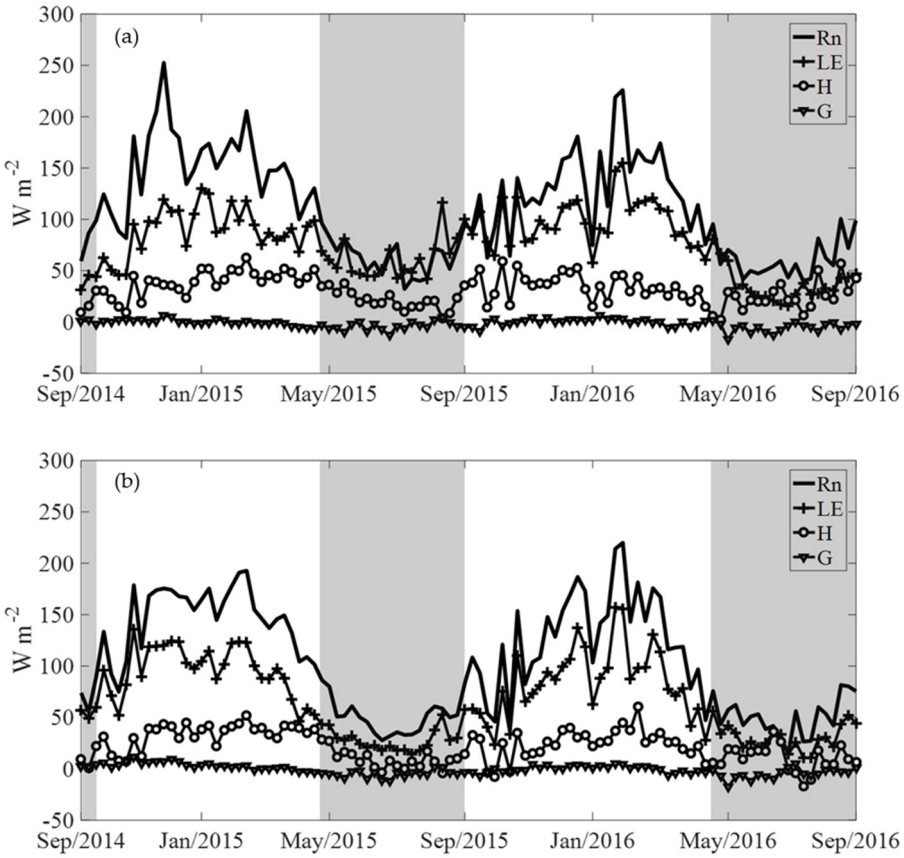

Figure 4. Weekly average of the energy balance components: net radiation, *Rn* (W m^{-2}); sensible heat flux, *H* (W m^{-2}); latent heat flux, *LE* (W m^{-2}); and soil heat flux, *G* (W m^{-2}) from 1 September 2014 to 1 September 2016, for the Pampa biome, at the (**a**) SMA and (**b**) PAS sites. The points represent the average every six days. The hatched areas represent the autumn-winter (AW) periods.

The annual *Rn* average presented similar values for both sites (Table 2), *Rn* values for AW being 47% and 39% smaller than SS in the SMA and PAS sites, respectively. Similar behavior and results were observed for *LE*. The *H* values were 62% and 54% smaller in AW than SS for SMA and PAS sites, respectively. Soil heat flux for both sites was generally negative in AW, and close to zero in SS. Therefore, in AW the subsurface heats the surface, while the opposite happens in SS. The smaller energy fluxes in AW are associated with smaller solar radiation in this period (Figure 2 and Table 2), coupled with a decrease in local vegetation (Figure 3) as also reported by Rajan et al. [16], Yunusa et al. [61] and Trepekli et al. [62].

In all analyzed periods, *LE* was higher than *H*, being $\beta < 1$ for both sites (Table 2). Lower values of β were found in the SS period for each site, while the highest values were found in AW. The PAS presented smaller β values than SMA, with less interannual variability. This difference in the flux partition may be related to the structure of the grassland vegetation at each site. Although the grassland vegetation of the Pampa biome is quite similar throughout the region, the SS is the highest biomass production period in the Pampa [63,64], responding locally to factors such as climate and soil. Thus, vegetation phenology in the Pampa biome also affects energy partitioning.

Figure 5 shows the average daily cycle of the energy balance components (*Rn*, *H*, *LE*, and *G*) for the SMA and PAS sites. In an annual daily cycle, the net radiation has a daily maximum of 425.0 W m^{-2} and 429.1 W m^{-2} for SMA and PAS, respectively. The values are negative between 18:30 and 6:30 local time. *Rn* was higher in SS, reaching a maximum of 547 W m^{-2}, while in AW, the maximum was 320 W m^{-2}.

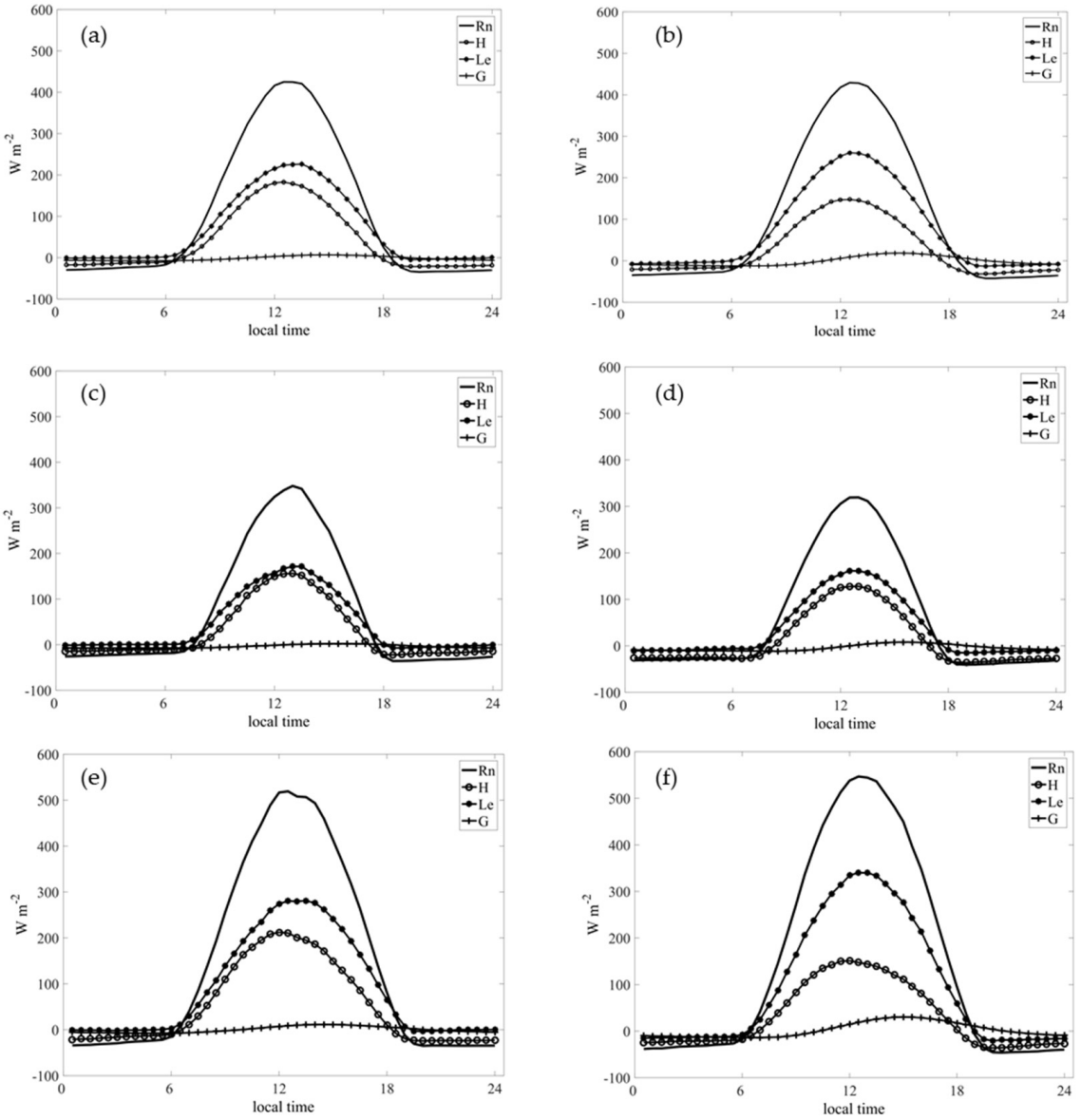

Figure 5. Daily cycle of the energy balance components, *Rn* (W m^{-2}); *H* (W m^{-2}); *LE* (W m^{-2}); *G* (W m^{-2}) for the SMA site on the left column and PAS on the right. (**a**,**b**) Average for the entire period; (**c**,**d**) AW; (**e**,**f**) SS.

LE reached a maximum of 226.3 W m^{-2} for SMA and 260.2 W m^{-2} for PAS in an annual daily cycle. Negative *LE* values were obtained in both sites at night, with more pronounced values for PAS, indicating the occurrence of condensation or dew formation during the night over most of the periods [55,65]. In AW, lower maximum values for *LE* were observed, reaching 48% and 61% of *LE* in SS, at the PAS and SMA sites, respectively. *LE* reverses its signal shortly after *Rn*. *VPD* is generally lower during the night when the air is colder, and increases during the day, when the air temperature is higher (Figure 2). *LE* increases throughout the day, with the beginning of the atmospheric convective processes, controlled by the net radiation. It reaches its maximum with higher air temperatures and decreases from the hottest period of the day due to the vegetation's biophysical conditions, closing the stomata to avoid water stress to the plants.

H shows little difference between the sites in their maximum and minimum values in the annual daily cycle. Its maximum was 147.6 W m^{-2} at noon, local time, for PAS and 182.9 W m^{-2} for SMA. In both sites, the *H* had a similar behavior between AW and SS. The difference between sites shows little influence of the available energy ($Rn - G$) in the range

of variation of *H*. Therefore, we can infer that the turbulence must be produced mainly by mechanical actions in PAS due to the greater wind speed (Figure 2), and less intensity by thermal convection, i.e., less air temperature (Figure 2). Comparing the AW and SS periods, the difference in the maximum amplitude values of *H* was of the order of 20 W m^{-2} and 56 W m^{-2} for the PAS and SMA sites, respectively.

G is near zero through the day in both sites. PAS presents *G* values slightly higher than the SMA site, possibly due to the soil type, which in PAS is sandy loam, allowing greater soil thermal conduction [66].

3.3. Environmental Variables That Control the H and LE Fluxes

The relationships between the environment variables (*Rg*, *Temp*, *RH*, and *VPD*) and *H* and *LE* for the SMA and PAS sites are shown in Table 3. The turbulent fluxes for both sites had a better correlation to *Rn*. *LE* and *Rg* correlation coefficients for the SMA and PAS sites have very similar values. The *LE* correlates better with *Rg* and *VPD*.

Table 3. Pearson's correlation (r) coefficients between the *LE* and *H* with environmental variables for the SMA and PAS sites, from 1 September 2014 to 1 September 2016, in a half-hour base with a *p*-value of 0.001.

Pearson's Correlation	PAS	SMA
LE vs. *Rg*	0.97	0.86
LE vs. *VPD*	0.66	0.65
LE vs. *Temp*	0.50	0.48
LE vs. *RH*	−0.59	−0.64
H vs. *Rg*	0.92	0.90
H vs. *VPD*	0.48	0.44
H vs. *Temp*	0.36	0.30
H vs. *RH*	−0.47	−0.50

The correlation between energy fluxes and air temperature showed different values for each flux analyzed in this study. For *LE*, the PAS site showed a better correlation with air temperature when compared to the SMA site, unlike the *H*, which has a small correlation and very close values for both sites. These results support that air temperature is an indirect controller of evapotranspiration through its effect on the *VPD* [67].

The results of this study for the Pampa biome showed that local microclimate plays an important role in the energy partition. The increase in *Rn* increases both *H* and *LE*. However, any increase is controlled by water vapor, since the values of Pearson's correlation coefficients showed that *H* and *LE* tend to increase with high evaporative demand (high *VPD*). Likewise, *H* and *LE* raise with the increase in air temperature. Unlike the Pampa biome, Majozi et al. [68], in a similar study over the Savannah biome, reported that the increase in *VPD* results in an increase in *H* and a decrease in *LE*.

3.4. Aerodynamic and Surface Conductances

3.4.1. Average Daily Cycles

The average daily cycle of *Cs* and *Ca* for the entire study period and AW and SS periods in the Pampa biome are shown in Figure 6. *Cs* curve pattern has a maximum before noon, of 11.9 mm s^{-1} and 17.5 mm s^{-1}, in SMA (9:00) and PAS (10:30), respectively. Alves and Pereira [69] reported that the sharp increase of *Cs* in the early morning hours is due to the stomatal opening caused by solar radiation incidence. In the afternoon, the decrease in *Cs* is presumably due to stomatal closure, associated with other microclimate variables that directly influence *Cs*, higher temperatures, and *VPD* (Figure 2). In a study in the Amazon Forest, Goulden et al. [70] reported a fall in *Cs* in the afternoon attributed to stomatal closure caused by a high-temperature effect on photosynthetic biochemistry, an intrinsic circadian rhythm, or a combination of the three effects. In the average daily cycle, the highest surface conductance value for PAS is 32% higher than *Cs* at the SMA site. Krishnan et al. [71]

found maximum daily values for surface conductance of 14 mm s^{-1} in a pasture area in North America. Liu and Feng [72] reported maximum daily values for *Cs* of 28.3 mm s^{-1} in degraded pasture areas in China. Wang et al. [73] also found similar *Cs* values in Australia, 15 mm s^{-1}. *Cs* was also studied in some Brazilian biomes. Rodrigues et al. [74] obtained a maximum *Cs* value of 12.6 mm s^{-1} in the Cerrado. Da Rocha et al. [31] obtained maximum daily values of 25 mm s^{-1} in a forest biome while Tan et al. [75] suggested for the maximum *Cs* of tropical forest a value of 24.8 ± 13.8 mm s^{-1}. Marques et al. [76], for Caatinga biome, found a similar behavior for the daily cycle of *Cs*, but with maximum values (3 and 5 mm s^{-1}) lower than those obtained here (10 and 20 mm s^{-1}).

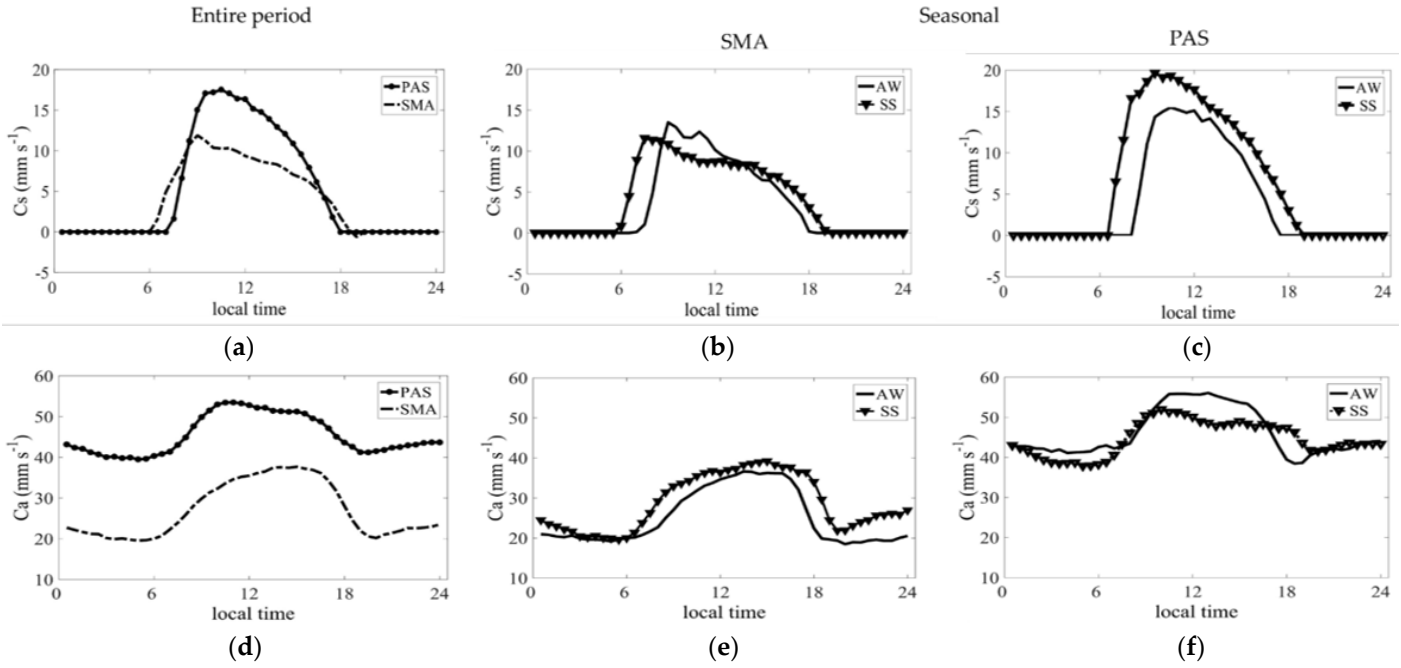

Figure 6. Average daily cycles of surface conductance (*Cs*, mm s^{-1}) (**a**–**c**) in top panels and aerodynamic conductance (*Ca*, mm s^{-1}) (**d**–**f**) in bottom panels for the Pampa biome, at the SMA and PAS sites, on the left column for the entire study period, on central for SMA in the AW and SS periods, and on right for PAS in the AW and SS periods.

Negative *Cs* values were observed before 6:30 and after 18:30 at the SMA site. For the PAS site, *Cs* has a longer interval, between 07:30 and 17:30, with negative values. According to Groh et al. [77] and Phillips and Oren [78], we assumed that *Cs* is zero for a wet canopy during the night period. Thus, water evaporates freely at its minimum rate, that is, without resistance to water vapor. When the canopy is dry, *Cs* is positive. When calculated using flux data from the eddy covariance method, *Cs* showed greater fluctuations during the day because the data obtained with this method exhibit relatively large fluctuations, especially when the local stability of atmospheric stratification changes in the early morning and late afternoon [57,79].

On average, for the entire study period, *Ca* reaches its maximum value at 11:00 at the SMA site and 15:00 at the PAS site. There is a significant difference in the peak hours of *Ca*, which is directly associated with the friction velocity that reaches its highest values at noon at the SMA site and 15:00 in PAS. The maximum values obtained for SMA and PAS are 37.7 mm s^{-1} and 53.5 mm s^{-1}, respectively, which represents a 30% difference between both sites. The differences in *Ca* between the sites can be attributed to the different wind speeds (Figure 2) since this variable is the main component in the calculation of aerodynamic conductance.

The analysis of *Cs* in the AW and SS periods (Figure 6) shows maximum values at the SMA site of 13.5 mm s^{-1} and 11.6 mm s^{-1}, respectively. In PAS, the values are higher, with

15.5 mm s^{-1} in AW and 19.7 mm s^{-1} in SS. Thus, the difference in *Cs* between the SMA and PAS sites is 13% in the AW period and 42% in the SS period. However, *Ca* differs between the SMA and PAS sites by 35% and 24% in the AW and SS periods, respectively. The maximum values obtained for *Ca* at the SMA site are 36.6 mm s^{-1} and 39.2 mm s^{-1} in the AW and SS periods, respectively. In PAS, the maximum values obtained are 56.1 mm s^{-1} in the AW and 52.0 mm s^{-1} in the SS. These values show a clear seasonal trend related to the weather and climate conditions of the study sites since both have native field ecosystems in the Pampa biome.

Patterns of seasonal variability in *Cs* and *Ca* have been observed in other studies, such as in the Amazon Forest [31] and Pantanal [29]. In the Cerrado, Cabral et al. [30] reported that *Cs* presented a strong seasonal variation of approximately 20 mm s^{-1} and 2 mm s^{-1} in rainy and dry seasons, respectively. However, *Ca* showed relatively small seasonal variation and the average between the dry and rainy seasons was 129 mm s^{-1}. Krishnan et al. [71] reported a significant seasonal and interannual variation in *Cs* similar to the changes that occurred in *ET* for pastures in North America.

In the AW and SS periods, *Cs* and *Ca* were directly related to the wind intensity, as verified by comparing Figure 6 and the different atmospheric variables presented in the average daytime cycle in Figure 2. *Cs*, which can be considered analogous to stomatal conductance, on a large scale, provides a useful measure of the effect of energy exchanges on plant physiology. *Cs* at the SMA site was higher in the AW period (Figure 6), which suggests that seasonal changes in *Cs* are strongly associated, in part, with changes in the leaf area index (LAI) or leaf physiology. The water flux between the leaf and atmosphere is high since the AW period tends to show no water restrictions at the site and the environmental conditions for the exchange of gases in the stomata are favorable.

Cs at the PAS site had its highest value in the SS period, which is consistent with the higher wind velocity in the AW and SS periods. The transfer of steam inside the canopy depends on the intensity of the wind, or indirectly on *Ca*, which, according to Grelle et al. [80], is a function of turbulence parameters. Higher values in the wind velocity are also favorable to the increase of evapotranspiration since the water vapor transfer process is facilitated due to the increase in *Ca* [81]. High wind velocity decreases the thickness of the boundary layer, allowing the stomatal resistance to control water loss. If the water in the soil (soil moisture) is less abundant, as is the case in PAS all year (Table 2), the stomata will open less or even remain closed on a sunny morning. Finally, the theory used to estimate the conductances, the "big-leaf" theory, combined with the method of estimating turbulent fluxes, eddy covariance, couples the plant surface with the atmosphere. Thus, vegetation cover near surface perceives the direct effects of turbulence during the day. Therefore, there is a need to develop empirical models that contemplate not only plant physiology (through stomata) but also a model that responds to all factors that control stomatal conductance.

3.4.2. Hysteresis Loops in the Surface Conductance

Cs responses to the main environmental variables (*Rn*, *VPD*, and *Temp*) for the average daily cycle throughout the study period are shown in Figure 7. These relationships form hysteresis loops, which had the directions followed in a clockwise direction for the three meteorological variables in both sites. The *Cs* values increased linearly in the morning, with an increase in *Rn*, *VPD*, and *Temp* at both sites. Table 4 shows the hour in which the hysteresis loops occurred for the meteorological variables at the maximum peak of the surface conductance. When reaching the maximum *Cs* peak, the available energy had not yet reached its maximum value. In other words, *Cs* decreased at midday with the increase in *Rn*. *Cs* decreases linearly with the decrease in *Rn* to its lowest value in the afternoon, reaching negative values at night.

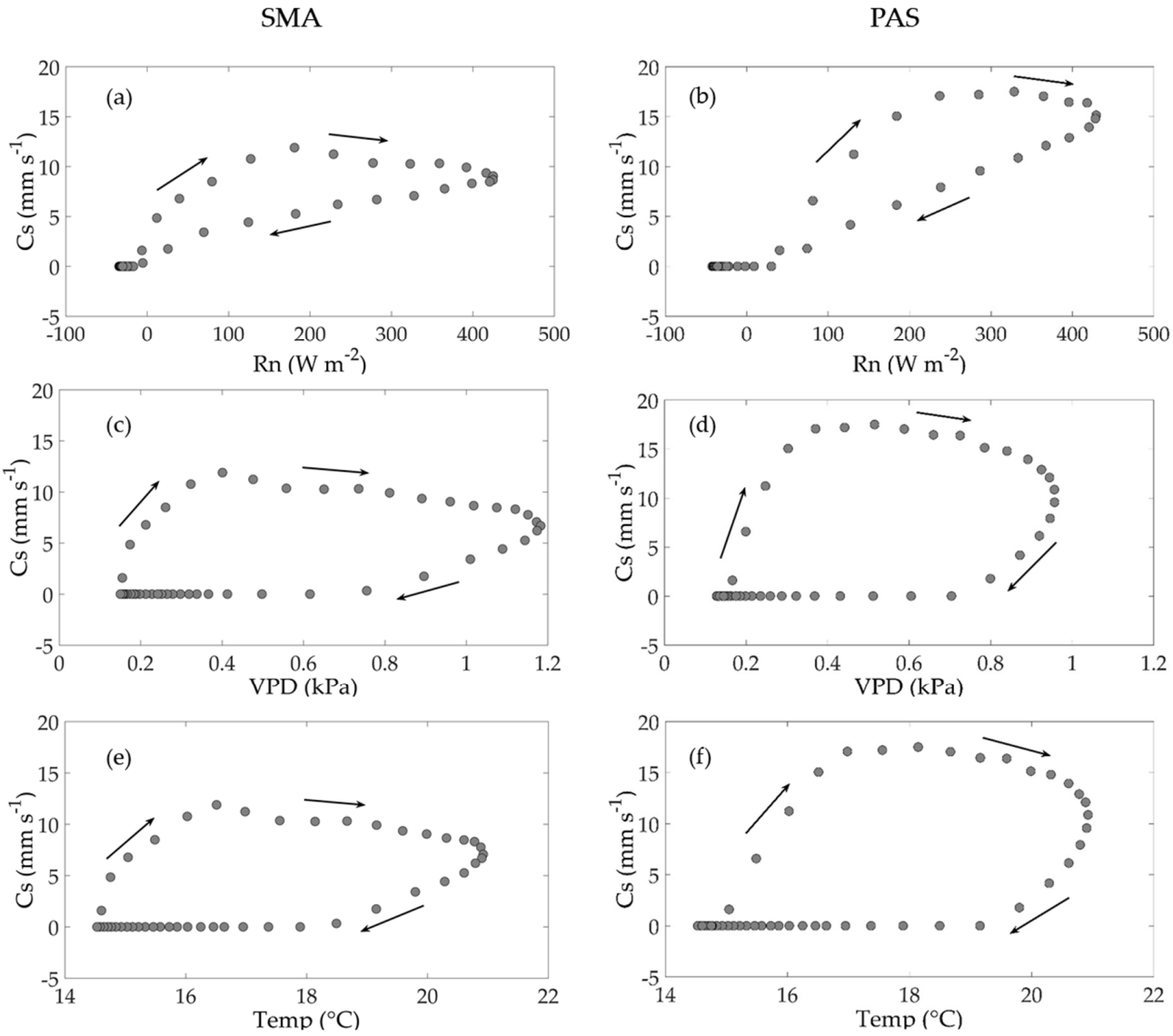

Figure 7. Hysteresis loops between surface conductance (*Cs*, mm s^{-1}) and the environmental variables of net radiation (*Rn*, W m^{-2}); vapor pressure deficit (*VPD*, kPa), and air temperature (*Temp*, °C) for the (**a**,**c**,**e**) SMA and (**b**,**d**,**f**) PAS sites, from 1 September 2014 to 1 September 2016.

Table 4. Maximum values and respective hour for the surface conductance *Cs* (mm s^{-1}), net radiation (*Rn*, W m^{-2}), air temperature (*Temp*, °C), and vapor pressure deficit (*VPD*, kPa) occur for the Pampa biome, at the SMA and PAS sites, in the average daily cycles, from 1 September 2014 to 1 September 2016.

Variables	Site	Max Value (Pick)	Hour	Values at Max *Cs*
Cs	SMA	11.9 mm s^{-1}	10 h 30 min	11.9 mm s^{-1}
	PAS	17.5 mm s^{-1}	9 h	17.5 mm s^{-1}
R_n	SMA	424.9 W m^{-2}	12 h 30 min	181.0 W m^{-2}
	PAS	429.1 W m^{-2}	12 h 30 min	328.4 W m^{-2}
VPD	SMA	1.182 kPa	15 h 30 min	0.40 kPa
	PAS	0.96 kPa	15 h 30 min	0.52 kPa
Temp	SMA	23.94 °C	15 h 30 min	16.5 °C
	PAS	20.92 °C	15 h	18.1 °C

The regressions between *Cs* and the environmental variables (*Rn*, *VPD*, and *Temp*) were determined to identify the main influencing factors on the surface conductance on a

daily scale throughout the study period. The Pearson's coefficients are presented in Table 5. *Rn* was the main influencing factor controlling *Cs* in the morning (P1—Table 5). However, the significant influence of air temperature on the surface conductance in the P1 period must be considered. The *VPD* and morning temperature directly influence the surface conductance in the afternoon. Therefore, we can infer that the behavior of opening or closing stomata can also contribute to the emergence of hysteresis.

Table 5. Pearson correlation (r) between the surface conductance *Cs* (mm s^{-1}), and the net radiation (*Rn*, W m^{-2}), air temperature (*Temp*, °C), and vapor pressure deficit (*VPD*, kPa) for the Pampa biome, at the SMA and PAS sites in periods P1 (06 h 30 min–11 h 30 min) and P2 (12 h–17 h), with a *p*-value of 0.001.

Variables		P1 (Morning)		P2 (Afternoon)	
		Cs		*Cs*	
		SMA	PAS	SMA	PAS
P1 (morning)	R_n	0.71	0.90	−0.98	−0.98
	VPD	0.65	0.82	−0.99	−1
	Temp	0.70	0.87	−0.98	−0.99
P2 (afternoon)	R_n	−0.49	−0.73	0.98	0.98
	VPD	0.96	0.92	−0.63	−0.56
	Temp	0.97	0.85	−0.61	−0.42

The gaps between the meteorological variables and *Cs* of the Pampa biome were more prominent at the PAS site. *Cs* in the afternoon (P2) was more linearly correlated with *VPD* and *Temp*, $r = -1$ and $r = -0.99$, respectively, which provides us with another important relationship to verify the limiting causes of *Cs*. While *VPD* or *Temp* increases, *Cs* tends to decrease since stomata must regulate their opening to prevent dehydration [82]. This fact is already known. However, the factors and intensities of these responses still require investigation. If there is a stomatal response to *VPD*, the mechanism that causes this response is still controversial [83]. According to Streck [83], two hypotheses proposed for this mechanism are discussed in the scientific community. The first, feedforward, is that stomatal conductance (*Ce*) decreases directly with the increase in *VPD*, with abscisic acid as the signal for the response. In the second hypothesis, feedback, *Ce* decreases with the increase in *VPD* due to the increase in leaf transpiration, which decreases the water potential in the leaf. Kelliher [84] reports that vegetation with LAI > 3 m^2 m^{-2} has minimal soil evaporation, allowing *Cs* to be a good approximation of the physiological parameter *Ce*. Thus, in this work, it was possible to verify the effect of *VPD* on the daily cycles of surface conductance and, in turn, the stomatic response to atmospheric demand.

The plant can undergo water stress with high *VPD*. Therefore, the stomata close in response to *VPD* as a self-protective mechanism to avoid high transpiration rates [85]. The Pampa vegetation, which had good water availability throughout the period [39], presented a decrease in *Cs* throughout the day just after 9:00 when *Rn*, *Temp*, and *VPD* have not yet reached their maximum values. In other words, the period in which the stomatal opening became narrower (*Cs* decreasing) was before the decline in meteorological variables. This was also reported in other studies [86–88], showing what directly caused the hysteresis loops between *Cs* and the weather variables during the day. Even so, explaining the causes of this phenomenon seems to be fraught with complex interactions between exogenous and endogenous factors for the plant system [89,90]. The stomatal response to *VPD* is still a subject of research in plant physiology [83].

3.5. Biophysical Control of Evapotranspiration

The relationships between *Cs* and *Ca* also formed hysteresis loops with *ET* in the average daily cycle and are shown in Figure 8. The relationship between *Ca* and *ET* for the PAS site showed a different behavior from the other relationships. In this cycle, the *ET*

response to *Ca* increase is high in the early morning. The same occurs after 17:00 when the *ET* drop ratio shows a quick response due to the *Ca* decrease. In other words, the hysteresis cycle may be negligible during these periods. Between 9:00 and 17:00, the formation of hysteresis loops between *ET* and *Ca* is counterclockwise and shows *ET* response to *Ca* when aerodynamic conductance values are already reducing. At 9:00 and 17:00, the *ET* reaches close values, ending the hysteresis cycle. At the SMA site, the relationship between aerodynamic conductance and *ET* forms clockwise hysteresis loops, showing that the *ET* response to *Ca* is high earlier in the day. At 13:00 (local time), the maximum *ET* value begins to drop the *Ca*, thereby decreasing *ET*. However, in this period, the *ET* response to *Ca* is lower when compared to the morning period. Therefore, between 13:00 and 15:00, ET shows less *Ca* dependence, showing high biophysical control in the evapotranspiration rate. Mallick et al. [91] report hysteresis loops between the *Cs* and *Ca* with evaporation and transpiration in the Amazon Basin. The authors reported significant hysteresis between the transpiration component and *Cs* during the dry season for sites with pasture vegetation. The evaporation component was significantly influenced by *Ca* for all sites.

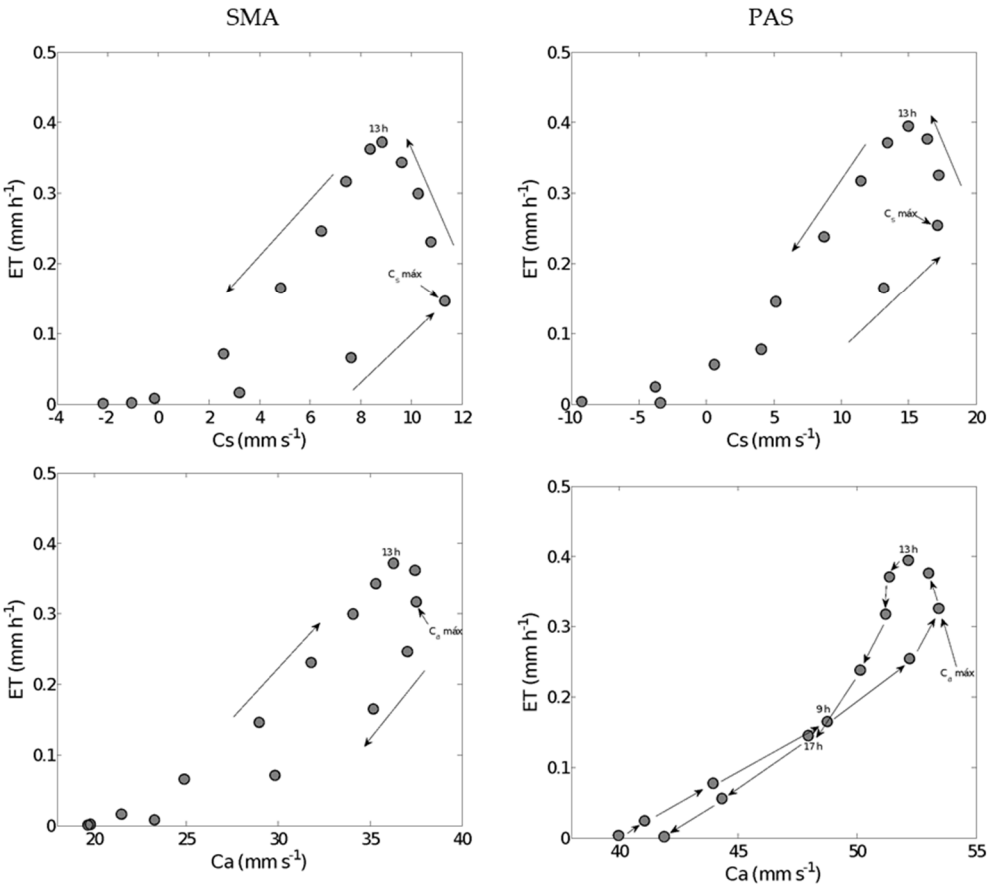

Figure 8. Hysteresis loops between surface conductance (*Cs*, mm s^{-1}), aerodynamic conductance (*Ca*, mm s^{-1}), and evapotranspiration (*ET*, mm h^{-1}) for the SMA and PAS sites, from 1 September 2014 to 1 September 2016.

The relationships between *ET* and surface conductance for both sites formed hysteresis loops in a counterclockwise direction, showing a low *ET* response in the morning. In this period, *ET* increases as *Cs* increases until reaching their maximum value at 9:00 at the SMA site and 11:00 in PAS. After this time, *Cs* begins to decrease with the increase in *ET*. Therefore, *ET* responds to *Cs* in this interval since evapotranspiration does not reduce instantly, even after the stomata have closed. In summary, the decrease in *ET* is mainly caused by the *Cs* reduction response due to the increase in *VPD* and air temperature.

The areas of the hysteresis curves were estimated to verify the intensity of *ET* response to *Cs* and Ca. Hysteresis was weaker in the *ET-Ca* ratios when compared to *ET-Cs*. The largest area obtained was for the *ET-Cs* ratio at the SMA site (0.0657), 33% higher than for the PAS site. The *ET-Ca* ratio was weaker at the PAS site, representing only 7% of the area's value for the same ratio at the SMA site. On average, ET responds more strongly to surface conductance, about 86%, compared to the Pampa biome *ET-Ca* ratio.

4. Conclusions

In this work, we assessed the patterns and controls in the turbulent energy exchanges of the Pampa biome in southern Brazil from two grassland sites. *Rn* presented a strong seasonality, with AW being 47% and 39% smaller than SS in the SMA and PAS sites, respectively. *LE* was the main component of the energy balance in AW and SS periods, but with similar results of *H* during AW in both sites. Global radiation was the main controller of the *LE* and *H*. *G* was a smaller component of the energy partition, with greater values in PAS.

Cs and *Ca* for both sites did not show seasonality. *Cs* and *Ca* were highly influenced by *u* and turbulence conditions in each site. *Rn* was the main driving factor controlling *Cs* in the morning. *VPD* and morning air temperature directly influenced *Cs* in the afternoon. *Cs* presented a similar daily cycle for both sites, with *Ca* showing a higher magnitude in PAS, mainly because of higher *u*. The hysteresis cycles formed by *ET* and the conductances showed substantial biophysical control in the *ET* process complex.

Cs and *Ca* are considered complex variables and have fundamental importance in most land surface models. In addition, the Pampa biome is a complex ecosystem where the surface–atmosphere interactions depend on weather and climate, soil, and vegetation phenology. Thus, the results presented in this study should guide numerical modeling simulations and public water use policies for Pampa biome ecosystem.

Author Contributions: G.C.D.R., V.d.A.S., T.Z., G.P.V., A.M. and T.B. collected, processed, and analyzed the eddy covariance data. G.C.D.R. and D.R.R. wrote the manuscript. D.R.R. and L.G.G.d.G. conceived and designed the experiments. D.R.R. supervised and advised all the research work that led to this paper. D.R.R., V.d.A.S., T.B., A.R. and L.G.G.d.G. reviewed the manuscript and conducted the English editing. All authors have read and agreed to the published version of the manuscript.

Funding: This study was financed in part by Coordination for the Improvement of Higher Education Personal (CAPES-Brazil) through the project CAPES-ANA-DPB (88881.178688/2018-01).

Institutional Review Board Statement: Not applicable.

Informed Consent Statement: Not applicable.

Acknowledgments: The authors acknowledge the National Council for Scientific and Technological Development (CNPq-Brazil), the Coordination for the Improvement of Higher Education Personnel (CAPES-Brazil), the Foundation for Research of Rio Grande do Sul State (FAPERGS, Project n° 17/2551-0001124-4), and Financier of Studies and Projects (FINEP-Brazil) for their financial support. The authors acknowledge the staff of the Micrometeorology Lab of the Federal University of Santa Maria (UFSM) for the technical support provided, particularly relative to the flux tower and the eddy covariance instruments. The authors acknowledge the Acevedo family for allowing us to carry out the experiment on their farm in Pedras Altas.

Conflicts of Interest: The authors declare no conflict of interest.

References

1. Sellers, P.J.; Bounoua, L.; Collatz, G.J.; Randall, D.A.; Dazlich, D.A.; Los, S.O.; Berry, J.A.; Fung, I.; Tucker, C.J.; Field, C.B.; et al. Comparison of Radiative and Physiological Effects of Doubled Atmospheric CO2 on Climate. *Science* **1996**, *271*, 1402–1406. [CrossRef]
2. Zhang, Y.; Kadota, T.; Ohata, T.; Oyunbaatar, D. Environmental controls on evapotranspiration from sparse grassland in Mongolia. *Hydrol. Process.* **2007**, *21*, 2016–2027. [CrossRef]
3. Woodward, F.I.; Smith, T.M. Global Photosynthesis and Stomatal Conductance: Modelling the Controls by Soil and Climate. *Adv. Bot. Res.* **1994**, *20*, 1–41.

4. Adams, J.M.; Faure, H.; Faure-Denard, L.; McGlade, J.M.; Woodward, F.I. Increases in terrestrial carbon storage from the Last Glacial Maximum to the present. *Nature* **1990**, *348*, 711–714. [CrossRef]
5. Roesch, L.F.W.; Vieira, F.C.B.; Pereira, V.A.; Schünemann, A.L.; Teixeira, I.F.; Senna, A.J.T.; Stefenon, V.M. The Brazilian Pampa: A fragile biome. *Diversity* **2009**, *1*, 182–198. [CrossRef]
6. Overbeck, G.; Muller, S.; Fidelis, A.; Pfadenhauer, J.; Pillar, V.; Blanco, C.; Boldrini, I.; Both, R.; Forneck, E. Brazil's neglected biome: The South Brazilian Campos. *Perspect. Plant Ecol. Evol. Syst.* **2007**, *9*, 101–116. [CrossRef]
7. Ruviaro, C.F.; de Léis, C.M.; Lampert, V.D.N.; Barcellos, J.O.J.; Dewes, H. Carbon footprint in different beef production systems on a southern Brazilian farm: A case study. *J. Clean. Prod.* **2015**, *96*, 435–443. [CrossRef]
8. Pillar, V.D.; Müller, S.C.; Castilhos, Z.M.; Jacques, A.V.Á. *Campos Sulinos—Conservação E Uso Sustentável Da Biodiversidade*; Ministério do Meio Ambiente: Brasília, Brazil, 2009; ISBN 978-85-7738-117-3.
9. Oliveira, T.E.D.; Freitas, D.S.D.; Gianezini, M.; Ruviaro, C.F.; Zago, D.; Mércio, T.Z.; Dias, E.A.; Lampert, V.D.N.; Barcellos, J.O.J. Agricultural land use change in the Brazilian Pampa Biome: The reduction of natural grasslands. *Land Use Policy* **2017**, *63*, 394–400. [CrossRef]
10. Chen, S.; Chen, J.; Lin, G.; Zhang, W.; Miao, H.; Wei, L.; Huang, J.; Han, X. Energy balance and partition in Inner Mongolia steppe ecosystems with different land use types. *Agric. For. Meteorol.* **2009**, *149*, 1800–1809. [CrossRef]
11. Babel, W.; Biermann, T.; Coners, H.; Falge, E.; Seeber, E.; Ingrisch, J.; Schleuß, P.-M.; Gerken, T.; Leonbacher, J.; Leipold, T.; et al. Pasture degradation modifies the water and carbon cycles of the Tibetan highlands. *Biogeosciences* **2014**, *11*, 6633–6656. [CrossRef]
12. Lan, X.; Li, Y.; Shao, R.; Chen, X.; Lin, K.; Cheng, L.; Gao, H.; Liu, Z. Vegetation controls on surface energy partitioning and water budget over China. *J. Hydrol.* **2021**, *600*, 125646. [CrossRef]
13. Lang, Y.; Yang, X.; Cai, H. Assessing the degradation of grassland ecosystems based on the advanced local net production scaling method—The case of Inner Mongolia, China. *Land Degrad. Dev.* **2021**, *32*, 559–572. [CrossRef]
14. Knapp, A.K.; Smith, M.D. Variation Among Biomes in Temporal Dynamics of Aboveground Primary Production. *Science* **2001**, *291*, 481–484. [CrossRef]
15. Guo, D.; Westra, S.; Maier, H.R. Impact of evapotranspiration process representation on runoff projections from conceptual rainfall-runoff models. *Water Resour. Res.* **2017**, *53*, 435–454. [CrossRef]
16. Rajan, N.; Maas, S.J.; Cui, S. Extreme drought effects on summer evapotranspiration and energy balance of a grassland in the Southern Great Plains. *Ecohydrology* **2015**, *8*, 1194–1204. [CrossRef]
17. Wang, K.; Dickinson, R.E. A review of global terrestrial evapotranspiration: Observation, modeling, climatology, and climatic variability. *Rev. Geophys.* **2012**, *50*, RG2005. [CrossRef]
18. Bonan, G.B. Forests and Climate Change: Forcings, Feedbacks, and the Climate Benefits of Forests. *Science* **2008**, *320*, 1444–1449. [CrossRef]
19. Senay, G.B.; Leake, S.; Nagler, P.L.; Artan, G.; Dickinson, J.; Cordova, J.T.; Glenn, E.P. Estimating basin scale evapotranspiration (ET) by water balance and remote sensing methods. *Hydrol. Process.* **2011**, *25*, 4037–4049. [CrossRef]
20. Forzieri, G.; Alkama, R.; Miralles, D.G.; Cescatti, A. Satellites reveal contrasting responses of regional climate to the widespread greening of Earth. *Science* **2017**, *356*, 1180–1184. [CrossRef]
21. Liu, Z.; Cheng, L.; Zhou, G.; Chen, X.; Lin, K.; Zhang, W.; Chen, X.; Zhou, P. Global Response of Evapotranspiration Ratio to Climate Conditions and Watershed Characteristics in a Changing Environment. *J. Geophys. Res. Atmos.* **2020**, *125*, e2020JD032371. [CrossRef]
22. Zha, T.; Li, C.; Kellomäki, S.; Peltola, H.; Wang, K.-Y.; Zhang, Y. Controls of Evapotranspiration and CO_2 Fluxes from Scots Pine by Surface Conductance and Abiotic Factors. *PLoS ONE* **2013**, *8*, e69027.
23. Igarashi, Y.; Kumagai, T.; Yoshifuji, N.; Sato, T.; Tanaka, N.; Tanaka, K.; Suzuki, M.; Tantasirin, C. Environmental control of canopy stomatal conductance in a tropical deciduous forest in northern Thailand. *Agric. For. Meteorol.* **2015**, *202*, 1–10. [CrossRef]
24. Hirano, T.; Suzuki, K.; Hirata, R. Energy balance and evapotranspiration changes in a larch forest caused by severe disturbance during an early secondary succession. *Agric. For. Meteorol.* **2017**, *232*, 457–468. [CrossRef]
25. Zhao, W.; Liu, B.; Chang, X.; Yang, Q.; Yang, Y.; Liu, Z.; Cleverly, J.; Eamus, D. Evapotranspiration partitioning, stomatal conductance, and components of the water balance: A special case of a desert ecosystem in China. *J. Hydrol.* **2016**, *538*, 374–386. [CrossRef]
26. Yue, P.; Zhang, Q.; Zhang, L.; Li, H.; Yang, Y.; Zeng, J.; Wang, S. Long-term variations in energy partitioning and evapotranspiration in a semiarid grassland in the Loess Plateau of China. *Agric. For. Meteorol.* **2019**, *278*, 107671. [CrossRef]
27. Baldocchi, D. A comparative study of mass and energy exchange rates over a closed C3 (wheat) and an open C4 (corn) crop: II. CO2 exchange and water use efficiency. *Agric. For. Meteorol.* **1994**, *67*, 291–321. [CrossRef]
28. Jarvis, P.G.; McNaughton, K.G. Stomatal Control of Transpiration: Scaling Up from Leaf to Region. *Adv. Ecol. Res.* **1986**, *15*, 1–49.
29. Fraga, C.I.D.M.; Sanches, L.; Pinto Junior, O.B.; Curado, L.F.A.; Gaio, D.C. Canopy Conductance, Aerodynamic Conductance and the Decoupling Coefficient in the Vochysia Divergens Pohl (Vochysiaceae) Forest in the Brazilian Pantanal. *Rev. Bras. Meteorol.* **2015**, *30*, 275–284. [CrossRef]
30. Cabral, O.M.R.; da Rocha, H.R.; Gash, J.H.; Freitas, H.C.; Ligo, M.A.V. Water and energy fluxes from a woodland savanna (cerrado) in southeast Brazil. *J. Hydrol. Reg. Stud.* **2015**, *4*, 22–40. [CrossRef]
31. da Rocha, H.R.; Goulden, M.L.; Miller, S.D.; Menton, M.C.; Pinto, L.D.V.O.; de Freitas, H.C.; e Silva Figueira, A.M. Seasonality Of Water And Heat Fluxes Over A Tropical Forest In Eastern Amazonia. *Ecol. Appl.* **2004**, *14*, 22–32. [CrossRef]

32. Eamus, D.; Cole, S. Diurnal and Seasonal Comparisons of Assimilation, Phyllode Conductance and Water Potential of Three Acacia and One Eucalyptus Species in the Wet-Dry Tropics of Australia. *Aust. J. Bot.* **1997**, *45*, 275. [CrossRef]
33. Wilson, K.B.; Baldocchi, D.D. Seasonal and interannual variability of energy fluxes over a broadleaved temperate deciduous forest in North America. *Agric. For. Meteorol.* **2000**, *100*, 1–18. [CrossRef]
34. Yu, G.-R.; Nakayama, K.; Lu, H.-Q. Responses of Stomatal Conductance in Field-grown Maize Leaves to Certain Environmental Factors over a Long Term. *J. Agric. Meteorol.* **1996**, *52*, 311–320. [CrossRef]
35. Wright, I.R.; Manzi, A.O.; da Rocha, H.R. Surface conductance of Amazonian pasture: Model application and calibration for canopy climate. *Agric. For. Meteorol.* **1995**, *75*, 51–70. [CrossRef]
36. Sellers, P.J.; Randall, D.A.; Collatz, G.J.; Berry, J.A.; Field, C.B.; Dazlich, D.A.; Zhang, C.; Collelo, G.D.; Bounoua, L. A Revised Land Surface Parameterization (SiB2) for Atmospheric GCMS. Part I: Model Formulation. *J. Clim.* **1996**, *9*, 676–705. [CrossRef]
37. Villalobos, F.J.; Testi, L.; Orgaz, F.; García-Tejera, O.; Lopez-Bernal, A.; González-Dugo, M.V.; Ballester-Lurbe, C.; Castel, J.R.; Alarcón-Cabañero, J.J.; Nicolás-Nicolás, E.; et al. Modelling canopy conductance and transpiration of fruit trees in Mediterranean areas: A simplified approach. *Agric. For. Meteorol.* **2013**, *171–172*, 93–103. [CrossRef]
38. Polhamus, A.; Fisher, J.B.; Tu, K.P. What controls the error structure in evapotranspiration models? *Agric. For. Meteorol.* **2013**, *169*, 12–24. [CrossRef]
39. Rubert, G.C.; Roberti, D.R.; Pereira, L.S.; Quadros, F.L.F.; Velho, H.F.D.C.; Moraes, O.L.L.D. Evapotranspiration of the Brazilian Pampa Biome: Seasonality and Influential Factors. *Water* **2018**, *10*, 1864. [CrossRef]
40. Peel, M.C.; Finlayson, B.L.; McMahon, T.A. Updated world map of the Köppen-Geiger climate classification. *Hydrol. Earth Syst. Sci.* **2007**, *11*, 1633–1644. [CrossRef]
41. IBGE. Mapas. Available online: http://mapas.ibge.gov.br/tematicos/solos (accessed on 26 June 2021).
42. dos Santos, A.B.; de Quadros, F.L.F.; Confortin, A.C.C.; Seibert, L.; Ribeiro, B.S.M.R.; Severo, P.D.O.; Casanova, P.T.; Machado, G.K.G. Morfogênese de gramíneas nativas do Rio Grande do Sul (Brasil) submetidas a pastoreio rotativo durante primavera e verão. *Ciência Rural* **2014**, *44*, 97–103. [CrossRef]
43. Quadros, F.L.F.; Pillar, V.D.P. Dinâmica vegetacional em pastagem natural submetida a tratamentos de queima e pastejo. *Ciência Rural* **2001**, *31*, 863–868. [CrossRef]
44. Timm, A.U.; Roberti, D.R.; Streck, N.A.; de Gonçalves, L.G.G.; Acevedo, O.C.; Moraes, O.L.; Moreira, V.S.; Degrazia, G.A.; Ferlan, M.; Toll, D.L. Energy Partitioning and Evapotranspiration over a Rice Paddy in Southern Brazil. *J. Hydrometeorol.* **2014**, *15*, 1975–1988. [CrossRef]
45. Diaz, M.B.; Roberti, D.R.; Carneiro, J.V.; Souza, V.D.A.; de Moraes, O.L.L. Dynamics of the superficial fluxes over a flooded rice paddy in southern Brazil. *Agric. For. Meteorol.* **2019**, *276–277*, 107650. [CrossRef]
46. Acevedo, O.C.; Moraes, O.L.L.; Degrazia, G.A.; Medeiros, L.E. Intermittency and the exchange of scalars in the nocturnal surface layer. *Bound.-Layer Meteorol.* **2006**, *119*, 41–55. [CrossRef]
47. Webb, E.K.; Pearman, G.I.; Leuning, R. Correction of flux measurements for density effects due to heat and water vapour transfer. *Q. J. R. Meteorol. Soc.* **1980**, *106*, 85–100. [CrossRef]
48. Gash, J.H.C.; Culf, A.D. Applying a linear detrend to eddy correlation data in realtime. *Bound.-Layer Meteorol.* **1996**, *79*, 301–306. [CrossRef]
49. Moncrieff, J.B.; Massheder, J.M.; de Bruin, H.; Elbers, J.; Friborg, T.; Heusinkveld, B.; Kabat, P.; Scott, S.; Soegaard, H.; Verhoef, A. A system to measure surface fluxes of momentum, sensible heat, water vapour and carbon dioxide. *J. Hydrol.* **1997**, *188–189*, 589–611. [CrossRef]
50. Moncrieff, J.; Clement, R.; Finnigan, J.; Meyers, T. Averaging, Detrending, and Filtering of Eddy Covariance Time Series. In *Handbook of Micrometeorology*; Kluwer Academic Publishers: Dordrecht, The Netherlands, 2004; pp. 7–31.
51. Mauder, M.; Foken, T. Impact of post-field data processing on eddy covariance flux estimates and energy balance closure. *Meteorol. Z.* **2006**, *15*, 597–609. [CrossRef]
52. Nakai, T.; Shimoyama, K. Ultrasonic anemometer angle of attack errors under turbulent conditions. *Agric. For. Meteorol.* **2012**, *162–163*, 14–26. [CrossRef]
53. Vickers, D.; Mahrt, L. Quality control and flux sampling problems for tower and aircraft data. *J. Atmos. Ocean. Technol.* **1997**, *14*, 512–526. [CrossRef]
54. Reichstein, M.; Falge, E.; Baldocchi, D.; Papale, D.; Aubinet, M.; Berbigier, P.; Bernhofer, C.; Buchmann, N.; Gilmanov, T.; Granier, A.; et al. On the separation of net ecosystem exchange into assimilation and ecosystem respiration: Review and improved algorithm. *Glob. Chang. Biol.* **2005**, *11*, 1424–1439. [CrossRef]
55. Wilson, K.B.; Baldocchi, D.D.; Aubinet, M.; Berbigier, P.; Bernhofer, C.; Dolman, H.; Falge, E.; Field, C.; Goldstein, A.; Granier, A.; et al. Energy partitioning between latent and sensible heat flux during the warm season at FLUXNET sites. *Water Resour. Res.* **2002**, *38*, 30-1–30-11. [CrossRef]
56. Leuning, R.; Cleugh, H.A.; Zegelin, S.J.; Hughes, D. Carbon and water fluxes over a temperate Eucalyptus forest and a tropical wet/dry savanna in Australia: Measurements and comparison with MODIS remote sensing estimates. *Agric. For. Meteorol.* **2005**, *129*, 151–173. [CrossRef]
57. Foken, T. The energy balance closure problem: An overview. *Ecol. Appl.* **2008**, *18*, 1351–1367. [CrossRef] [PubMed]
58. Allen, R.G.; Pereira, L.S.; Raes, D.; Smith, M. *Crop Evapotranspiration-Guidelines For Computing Crop Water Requirements—FAO Irrigation And Drainage Paper 56*; FAO: Rome, Italy, 1998.

59. Campbell, G.S.; Norman, J.M. *An Introduction to Environmental Biophysics*; Springer: New York, NY, USA, 1998; ISBN 978-0-387-94937-6.
60. Lyra, G.B.; Pereira, A.R. Dificuldades de estimativa dos parâmetros de rugosidade aerodinâmica pelo perfil logarítmico do vento sobre vegetação esparsa em região semi-árida. *Rev. Bras. Geofísica* **2007**, *25*. [CrossRef]
61. Yunusa, I.A.M.; Eamus, D.; Taylor, D.; Whitley, R.; Gwenzi, W.; Palmer, A.R.; Li, Z. Partitioning of turbulent flux reveals contrasting cooling potential for woody vegetation and grassland during heat waves. *Q. J. R. Meteorol. Soc.* **2015**, *141*, 2528–2537. [CrossRef]
62. Trepekli, A.; Loupa, G.; Rapsomanikis, S. Seasonal evapotranspiration, energy fluxes and turbulence variance characteristics of a Mediterranean coastal grassland. *Agric. For. Meteorol.* **2016**, *226–227*, 13–27. [CrossRef]
63. Kuplich, T.M.; Moreira, A.; Fontana, D.C. Série temporal de índice de vegetação sobre diferentes tipologias vegetais no Rio Grande do Sul. *Rev. Bras. Eng. Agrícola E Ambient.* **2013**, *17*, 1116–1123. [CrossRef]
64. Guerini Filho, M.; Kuplich, T.M.; Quadros, F.L.F. De Estimating natural grassland biomass by vegetation indices using Sentinel 2 remote sensing data. *Int. J. Remote Sens.* **2020**, *41*, 2861–2876. [CrossRef]
65. Wilson, K.; Goldstein, A.; Falge, E.; Aubinet, M.; Baldocchi, D.; Berbigier, P.; Bernhofer, C.; Ceulemans, R.; Dolman, H.; Field, C.; et al. Energy balance closure at FLUXNET sites. *Agric. For. Meteorol.* **2002**, *113*, 223–243. [CrossRef]
66. Zimmer, T.; Buligon, L.; de Arruda Souza, V.; Romio, L.C.; Roberti, D.R. Influence of clearness index and soil moisture in the soil thermal dynamic in natural pasture in the Brazilian Pampa biome. *Geoderma* **2020**, *378*, 114582. [CrossRef]
67. Seneviratne, S.I.; Corti, T.; Davin, E.L.; Hirschi, M.; Jaeger, E.B.; Lehner, I.; Orlowsky, B.; Teuling, A.J. Investigating soil moisture–climate interactions in a changing climate: A review. *Earth-Sci. Rev.* **2010**, *99*, 125–161. [CrossRef]
68. Majozi, N.P.; Mannaerts, C.M.; Ramoelo, A.; Mathieu, R.; Nickless, A.; Verhoef, W. Analysing surface energy balance closure and partitioning over a semi-arid savanna FLUXNET site in Skukuza, Kruger National Park, South Africa. *Hydrol. Earth Syst. Sci.* **2017**, *21*, 3401–3415. [CrossRef]
69. Alves, I.; Santos Pereira, L. Modelling surface resistance from climatic variables? *Agric. Water Manag.* **2000**, *42*, 371–385. [CrossRef]
70. Goulden, M.L.; Miller, S.D.; da Rocha, H.R.; Menton, M.C.; de Freitas, H.C.; de Silva Figueira, A.M.; de Sousa, C.A.D. Diel and seasonal patterns of tropical forest CO_2 exchange. *Ecol. Appl.* **2004**, *14*, 42–54. [CrossRef]
71. Krishnan, P.; Meyers, T.P.; Scott, R.L.; Kennedy, L.; Heuer, M. Energy exchange and evapotranspiration over two temperate semi-arid grasslands in North America. *Agric. For. Meteorol.* **2012**, *153*, 31–44. [CrossRef]
72. Huizhi, L.; Jianwu, F. Seasonal and Interannual Variations of Evapotranspiration and Energy Exchange over Different Land Surfaces in a Semiarid Area of China. *J. Appl. Meteorol. Climatol.* **2012**, *51*, 1875–1888. [CrossRef]
73. Wang, H.; Guan, H.; Deng, Z.; Simmons, C.T. Optimization of canopy conductance models from concurrent measurements of sap flow and stem water potential on Drooping Sheoak in South Australia. *Water Resour. Res.* **2014**, *50*, 6154–6167. [CrossRef]
74. Rodrigues, T.R.; Vourlitis, G.L.; Lobo, F.D.A.; Santanna, F.B.; de Arruda, P.H.Z.; Nogueira, J.D.S. Modeling canopy conductance under contrasting seasonal conditions for a tropical savanna ecosystem of south central Mato Grosso, Brazil. *Agric. For. Meteorol.* **2016**, *218–219*, 218–229. [CrossRef]
75. Tan, Z.-H.; Zhao, J.-F.; Wang, G.-Z.; Chen, M.-P.; Yang, L.-Y.; He, C.-S.; Restrepo-Coupe, N.; Peng, S.-S.; Liu, X.-Y.; da Rocha, H.R.; et al. Surface conductance for evapotranspiration of tropical forests: Calculations, variations, and controls. *Agric. For. Meteorol.* **2019**, *275*, 317–328. [CrossRef]
76. Marques, T.V.; Mendes, K.; Mutti, P.; Medeiros, S.; Silva, L.; Perez-Marin, A.M.; Campos, S.; Lúcio, P.S.; Lima, K.; dos Reis, J.; et al. Environmental and biophysical controls of evapotranspiration from Seasonally Dry Tropical Forests (Caatinga) in the Brazilian Semiarid. *Agric. For. Meteorol.* **2020**, *287*, 107957. [CrossRef]
77. Groh, J.; Pütz, T.; Gerke, H.H.; Vanderborght, J.; Vereecken, H. Quantification and Prediction of Nighttime Evapotranspiration for Two Distinct Grassland Ecosystems. *Water Resour. Res.* **2019**, *55*, 2961–2975. [CrossRef]
78. Phillips, N.; Oren, R. A comparison of daily representations of canopy conductance based on two conditional time-averaging methods and the dependence of daily conductance on environmental factors. *Ann. Des. Sci. For.* **1998**, *55*, 217–235. [CrossRef]
79. Moffat, A.M.; Papale, D.; Reichstein, M.; Hollinger, D.Y.; Richardson, A.D.; Barr, A.G.; Beckstein, C.; Braswell, B.H.; Churkina, G.; Desai, A.R.; et al. Comprehensive comparison of gap-filling techniques for eddy covariance net carbon fluxes. *Agric. For. Meteorol.* **2007**, *147*, 209–232. [CrossRef]
80. Grelle, A.; Lindroth, A.; Mölder, M. Seasonal variation of boreal forest surface conductance and evaporation. *Agric. For. Meteorol.* **1999**, *98–99*, 563–578. [CrossRef]
81. Souza Filho, J.D.D.C.; Ribeiro, A.; Costa, M.H.; Cohen, J.C.P. Mecanismos de controle da variação sazonal da transpiração de uma floresta tropical no nordeste da amazônia. *Acta Amaz.* **2005**, *35*, 223–229. [CrossRef]
82. Grossiord, C.; Buckley, T.N.; Cernusak, L.A.; Novick, K.A.; Poulter, B.; Siegwolf, R.T.W.; Sperry, J.S.; McDowell, N.G. Plant responses to rising vapor pressure deficit. *New Phytol.* **2020**, *226*, 1550–1566. [CrossRef]
83. Streck, N.A. Stomatal response to water vapor pressure deficit: An unsolved issue. *Rev. Bras. Agrociência* **2003**, *09*, 314–322.
84. Kelliher, F.M.; Leuning, R.; Raupach, M.R.; Schulze, E.-D. Maximum conductances for evaporation from global vegetation types. *Agric. For. Meteorol.* **1995**, *73*, 1–16. [CrossRef]
85. Chen, L.; Zhang, Z.; Li, Z.; Tang, J.; Caldwell, P.; Zhang, W. Biophysical control of whole tree transpiration under an urban environment in Northern China. *J. Hydrol.* **2011**, *402*, 388–400. [CrossRef]

86. Lu, P.; Yunusa, I.A.M.; Walker, R.R.; Müller, W.J. Regulation of canopy conductance and transpiration and their modelling in irrigated grapevines. *Funct. Plant Biol.* **2003**, *30*, 689. [CrossRef]
87. Unsworth, M.; Phillips, N.; Link, T.; Bond, B.; Falk, M.; Harmon, M.; Hinckley, T.; Marks, D.; Paw, U. Components and Controls of Water Flux in an Old-growth Douglas-fir?Western Hemlock Ecosystem. *Ecosystems* **2004**, *7*, 468–481. [CrossRef]
88. Bai, Y.; Zhu, G.; Su, Y.; Zhang, K.; Han, T.; Ma, J.; Wang, W.; Ma, T.; Feng, L. Hysteresis loops between canopy conductance of grapevines and meteorological variables in an oasis ecosystem. *Agric. For. Meteorol.* **2015**, *214–215*, 319–327. [CrossRef]
89. Tuzet, A.; Perrier, A.; Leuning, R. A coupled model of stomatal conductance, photosynthesis and transpiration. *Plant. Cell Environ.* **2003**, *26*, 1097–1116. [CrossRef]
90. Zhang, Q.; Manzoni, S.; Katul, G.; Porporato, A.; Yang, D. The hysteretic evapotranspiration-Vapor pressure deficit relation. *J. Geophys. Res. Biogeosciences* **2014**, *119*, 125–140. [CrossRef]
91. Mallick, K.; Trebs, I.; Boegh, E.; Giustarini, L.; Schlerf, M.; Drewry, D.T.; Hoffmann, L.; von Randow, C.; Kruijt, B.; Araùjo, A.; et al. Canopy-scale biophysical controls of transpiration and evaporation in the Amazon Basin. *Hydrol. Earth Syst. Sci.* **2016**, *20*, 4237–4264. [CrossRef]